Nb2O5/TiO2 heterojunctions: Synthesis strategy and photocatalytic activity

Junqing Yan, Guangjun Wu, Naijia Guan, Landong Li[*]

Key Laboratory of Advanced Energy Materials Chemistry (Ministry of Education), College of Chemistry, Nankai University, Tianjin 300071, PR China

ARTICLE INFO

ABSTRACT

In the present study, *in situ* hydrolysis-loading of ultra-fine niobium oxide nanoparticles on the surface of rutile TiO_2 is developed as a new strategy to synthesize Nb_2O_5/TiO_2 heterojunctions. The physico-chemical properties of Nb_2O_5/TiO_2 heterojunctions are fully characterized by X-ray diffraction, Raman, UV–vis, X-ray photoelectron spectroscopy and transmission electron microscopy. The separation effi-ciency of photo-generated electron–hole pairs on Nb_2O_5/TiO_2 heterojunctions under irradiation is investigated by photoluminescence and electron spin resonance spectroscopy. The activity of Nb_2O_5/TiO_2 heterojunctions is examined in the selective photocatalytic oxidation of α-phenylethanol and the pho-tocatalytic reforming of methanol. In both reactions, Nb_2O_5/TiO_2 heterojunctions exhibit distinct higher photocatalytic activity than pure rutile TiO_2 or Nb_2O_5. The photocatalytic activity of Nb_2O_5/TiO_2 hetero-junctions is relevant with Nb/Ti ratio and the optimal activity is obtained at Nb/Ti = 0.12 with the highest separation efficiency of photo-generated electron–hole pairs. Integrating the physico-chemical and pho-tocatalytic properties, the factors controlling the photocatalytic activity of Nb_2O_5/TiO_2 heterojunctions are discussed in detail.

© 2014 Elsevier B.V. All rights reserved.

1. Introduction

As a potential process to deal with energy crisis and envi-ronmental issues, heterogeneous photocatalysis, known since the 1970s [1], has drawn great attention in the past decades. In hetero-geneous photocatalysis, holes in the valence band and electrons in the conducting band are created when the semiconductors are illu-minated by photons with energy higher than their band gap. The holes in the valence band are powerful oxidants and the electrons in the conducting band are efficient reductants. Therefore, the photo-generated hole–electron pairs can act as redox centres to initiate photocatalytic reactions [2,3].

TiO_2 is the initial semiconductor photocatalyst investigated, and is still regarded as a benchmark photocatalyst under ultraviolet irradiation. TiO_2 shows several great advantages as photocata-lyst, such as good chemical stability, non-toxicity and commercial availability. However, the recombination rate of photo-generated hole–electron pairs on TiO_2 is very high, which greatly reduces the photocatalytic efficiency and limits the industrial applica-tion of TiO_2 [4,5]. To address this concern, several strategies have been proposed in the research of TiO_2 photocatalysis, *e.g.* loading some amounts of metal or metal oxide, known as

co-catalyst, on the surface of TiO_2 [6,7], or combining of TiO_2 with another semiconductor to form heterojunction [8–10]. For these two strategies, the inhibitory effects on recombination of photo-generated hole–electron pairs mainly come from the different Fermi level between TiO_2 and co-catalyst or another semiconductor.

Different types of heterojunctions, *e.g.* $WO_3/BiVO_4$ [11], CdS/TiO_2 [12], $Ag_3PO_4/BiVO_4$ [13] and organic semiconductor het-erostructures [14], have been prepared and successfully applied in photocatalysis. In principle, the creation of efficient tight junctions between two semiconductors depends greatly on the synthesis strategy [13]. Delicate design of heterojunctions, *e.g.* layer-by-layer of WO_3 and $BiVO_4$ heterojunction electrodes [11] and $CaFe_2O_4$ overlayer onto TaON electrode with intimate contact [8], has been proved to be effective to improve the photocatalytic or photoelec-trocatalytic activity. Recently, loading ultra-small semiconductor particles on another bulk semiconductor to create heterostruc-tural photocatalysts has been developed to accelerate the charge transfer between the two semiconductor components [15–18]. In this regard, *in situ* creating heterojunction system is reported [13,15,16]. For example, Liu et al. *in situ* loaded ultra-small (*ca.* 2 nm) Cu_2O particles on TiO_2 nanosheets and the as-prepared Cu_2O/TiO_2 exhibited photocatalytic activity *ca.* 3 times higher than $N-TiO_2$ [16]. Yao et al. *in situ* deposited Ag_3PO_4 nanoparticles onto the TiO_2 surface and Ag_3PO_4/TiO_2 exhibited excellent photocat-alytic activity [15]. For the *in situ* loading small particles on bulk

* Corresponding author. Tel.: +86 2223500341.
  E-mail address: lild@nankai.edu.cn (L. Li).

semiconductor, certain conditions are required for the heterogeneous nucleation, *e.g.* the accurate control of the pH value of the solution [15].

Nb_2O_5 is n-type transition metal oxide semiconductor with a bad gap of *ca.* 3.2 eV and it has been widely used in photocatalysis [19–22]. Nb_2O_5, like TiO_2, exhibits good chemical stability, non-toxicity and commercial availability. Therefore, Nb_2O_5/TiO_2 system can be expected as promising composite photocatalyst for application in industrial photocatalysis. To the best of our knowledge, the Nb_2O_5/TiO_2 heterojunction photocatalyst has not been well studied yet. In the present work, we will report the successful synthesis of ultra-fine Nb_2O_5 on rutile TiO_2 via *in situ* hydrolysis-loading under strong acidic conditions and the photocatalytic application of the as-prepared Nb_2O_5/TiO_2 heterojunctions.

2. Experimental

2.1. Sample preparation

Titanium isopropoxide, isopropanol, niobium(V) chloride (99.9%), benzotrifluoride and α-phenylethanol were analytical grade and purchased from Alfa Aesar. Nitric acid (26–28 wt%) and hydrochloric acid (36–38%) were provided by Tianjin Guangfu Fine Chemical Research Institute. All the chemical reagents were used as received without further purification. Distilled water was used in the whole experiments.

Synthesis of rutile TiO_2 nanoparticles: Rutile TiO_2 nanoparticles were synthesized according to previous literature report [23]. Typically, 5 mL of titanium isopropoxide and 5 mL of dry isopropanol were mixed and stirred for 30 min. Then, the solution was added to 40 mL nitric acid solution (pH = 0.5). The mixture was heated at 80 °C for 10 h under stirring and the resulting solution was transferred into a 50 mL Teflon-lined autoclave for static crystallization (200 °C for 24 h). The white precipitates were washed thoroughly with distill water and ethanol, and dried at 80 °C overnight. The obtained TiO_2 powders were annealed at 450 °C for 4 h in air before further use.

Synthesis of Nb_2O_5/rutile-TiO_2 heterojunctions: 0.5 g rutile TiO_2 nanoparticles were dispersed in 30 mL 0.5 M hydrochloric acid solution and the resulting mixture was sonicated for 30 min. Then, a certain amount of $NbCl_5$ was added to the mixture under stirring. The homogeneously dispersed solution was heated at 100 °C to obtain the resulting off-white powders. The powders were dried in 80 °C for 24 h and Nb_2O_5/Rutile-TiO_2 heterojunctions were prepared as final products. The products are denoted as Nb/Ti = *n*, where *n* represents the mass ratio of Nb relative to Ti.

Pure Nb_2O_5 was also prepared through similar process and used as reference sample.

2.2. Sample characterization

The X-ray diffraction (XRD) patterns of samples were recorded on a Bruker D8 ADVANCE powder diffractometer using Cu-Kα radiation ($\lambda = 0.1542$ nm) at a scanning rate of 4 min^{-1} in the region of $2\theta = 10$–$80°$.

The specific surface areas of samples were determined through low temperature N_2 adsorption/desorption isotherms collected on a Quantachrome iQ-MP gas adsorption analyzer.

Transmission electron microscopy (TEM) images were taken on a Philips Tecnai G^2 20 S-TWIN electron microscope at an acceleration voltage of 200 kV. A few drops of alcohol suspension containing the sample were placed on a carbon-coated copper grid, followed by evaporation at ambient temperature.

Raman analysis was carried out on a Renishaw InVia Raman spectrometer and spectra were obtained with the green line of an Ar-ion laser (514.53 nm) in micro-Raman configuration.

Diffuse reflectance ultraviolet–visible (UV–Vis) spectra of diluted samples (diluted in $BaSO_4$ at a ratio of 1:9) were recorded in the air against $BaSO_4$ in the region of 200–700 nm on a Varian Cary 300 UV–vis spectrophotometer.

X-ray photoelectron spectra (XPS) were recorded on a Kratos Axis Ultra DLD spectrometer with a monochromated Al-Kα X-ray source ($h\nu = 1486.6$ eV), hybrid (magnetic/electrostatic) optics and a multi-channel plate and delay line detector (DLD). All spectra were recorded by using an aperture slot of 300×700 microns, survey spectra were recorded with a pass energy of 160 eV and high-resolution spectra with a pass energy of 40 eV. Accurate binding energies (± 0.1 eV) were determined with respect to the position of the adventitious C 1s peak at 284.8 eV.

Photoluminescence (PL) spectra were recorded on a Spex FL201 fluorescence spectrophotometer. The samples were dry-pressed into self-supporting wafers and then illuminated by 325 nm He-Cd laser as excitation source at ambient temperature.

Electron spin resonance (ESR) was carried out on a Bruker A300 instrument with a microwave power of 5.0 mW and a modulation frequency of 100 kHz. 2,2-Diphenyl-1-picrylhydrazyl hydrate (DPPH) was used as an internal standard for the measurement of the magnetic field. In a typical experiment, sample of 0.15 g was placed in a quartz ESR tube and evacuated at 473 K for 2 h. After cooled down to 298 K, 50 Torr O_2 was introduced to the cube and kept for 15 min. The excess amount of O_2 was removed from the tube by evacuation for 10 min and then the tube was analyzed at 100 K in dark or under UV–vis light irradiation.

Mott-Schottky plots were measured using a three-electrode cell electrochemical workstation (IVIUM CompactStat). The saturated Ag/AgCl and platinum foil (2×2 cm^2) were used as the reference electrode and the counter electrode. The sample (1 mg) was dispersed in 1 mL anhydrous ethanol and then evenly grinded to slurry. The slurry was spread onto ITO glass and the exposed area was kept at 0.25 cm^2. The prepared ITO/samples was dried overnight under ambient conditions and then used as the working electrode. The measurements were obtained at a fixed frequency of 1 kHz in 0.5 M Na_2SO_4 solution in the dark.

2.3. Photocatalytic evaluation

The photocatalytic oxidation of α-phenylethanol was performed in a top-irradiation-type double-walled quartz cell cooled by water with a Xe lamp (200 W, wavelength: 320–780 nm) as a light source. In each experiment, the catalyst of *ca.* 0.3 g was dispersed in the mixture of benzotrifluoride (solvent) and 25 mmol α-phenylethanol (or other alcohol) in the quartz cell under stirring. The suspension was then irradiated with air bubbled in at *ca.* 20 mL/min. The organic products were analyzed by GC (Shimadzu GC-2010 Plus) and GC-MS (Shimadzu GCMS-QP2010 SE). Meanwhile, an absorption apparatus containing saturated $Ba(OH)_2$ solution was equipped at down-stream of quartz cell to determine the quantity of CO_2 that might form during reaction.

Photocatalytic reforming of methanol (also-known as photocatalytic water splitting with methanol as sacrificial agent) was performed in a top-irradiation-type Pyrex reaction cell connected to a closed gas circulation and evacuation system under the irradiation of Xe lamp (wavelength: 320–780 nm). In a typical experiment, catalyst sample of 100 mg was suspended in 100 mL 10% methanol aqueous solution in the reaction cell. After evacuated for 30 min, the reactor cell was irradiated by the Xe lamp at 200 W under stirring. The gaseous products were analyzed by an on-line gas chromatograph (Varian CP-3800) with thermal conductivity
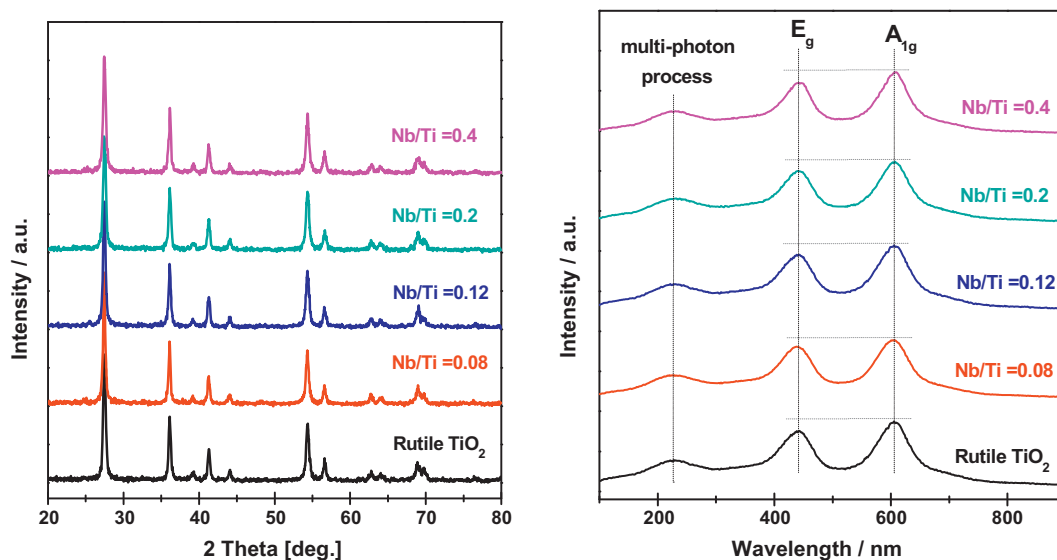
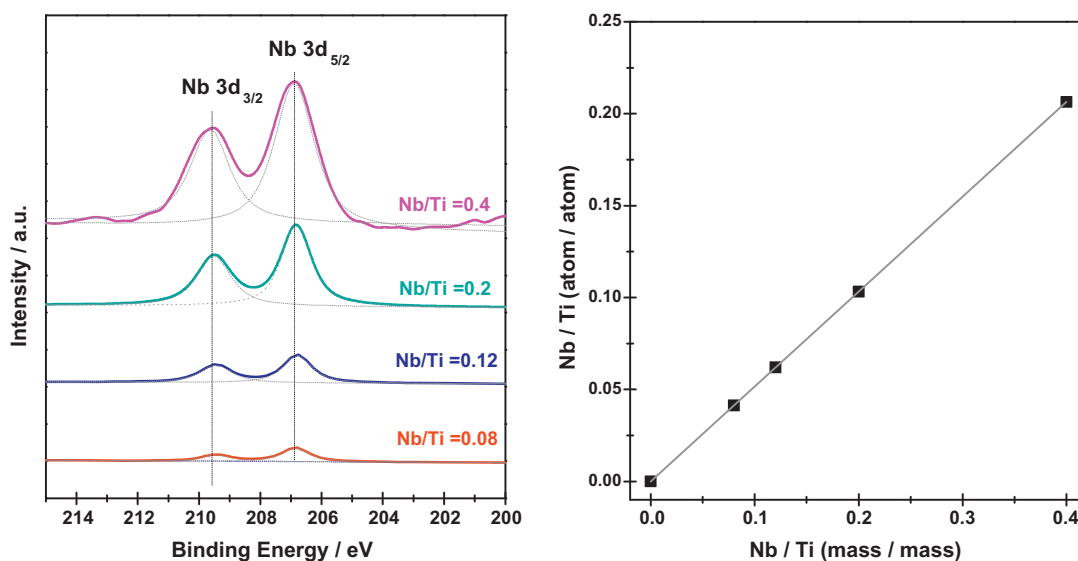**Fig. 1.** XRD (left) and Raman (right) patterns of rutile TiO_2 and Nb_2O_5/TiO_2 heterojunctions.

Fig. 2. XPS (left) and surface niobium loadings (right) of Nb_2O_5/TiO_2 heterojunctions.

detector. For all photocatalyst samples, 1% Pt was *in situ* photo-deposited from H_2PtCl_6 solution.

3. Results and discussion

3.1. Formation and characterization of Nb_2O_5/TiO_2 heterojunctions

The phase structure of rutile TiO_2 and Nb_2O_5/TiO_2 heterojunctions are characterized by XRD and Raman spectroscopy. As shown in Fig. 1 (left), the typical diffraction patterns of rutile TiO_2 (JCPDF# 21-1276) are observed for TiO_2 and Nb_2O_5/TiO_2 heterojunctions. Besides, no diffraction peaks corresponding to niobium species could be observed, which should be due to the high dispersion of niobium species and their amorphous state (Fig. S1) [20,22]. On the other hand, the intensities and shapes of diffraction peaks are quite similar, and the average particle sizes are calculated to *ca.* 30 nm for all samples according to the Scherer equation from the broadening of rutile (110) reflection ($2\theta = 27.5$). Raman spectra

are further employed to identify the surface geometric structure of the samples. As shown in Fig. 1 (right), three Raman-active modes corresponding to the typical vibrational bands of rutile TiO_2 [24] are clearly observed for TiO_2 and Nb_2O_5/TiO_2 heterojunctions. The absence of Raman-active modes corresponding to niobium oxides in Nb_2O_5/TiO_2 heterojunctions indicates that Nb_2O_5 is amorphous. Moreover, the unchanged Raman-active modes before and after Nb_2O_5 loading suggest that loading of Nb_2O_5 on TiO_2 do not influence the surface structure of rutile TiO_2.

The existence states of niobium species and surface elemental composition in Nb_2O_5/TiO_2 heterojunctions are investigated by means of XPS and the results are shown in Fig. 2. Ti, O and Nb are detected as exclusive elements in Nb_2O_5/TiO_2 heterojunctions (Fig. S2), ruling out the possible influences from impurities. In Nb 3d region, the binding energy values at 207.1 and 209.9 eV are observed for pure Nb_2O_5 sample (Fig. S3), confirming that amorphous Nb_2O_5 is obtained as reference sample. While for Nb_2O_5/TiO_2 heterojunctions, the binding energy values at 206.9 and 209.7 eV are observed, which are *ca.* 0.2 eV lower than reference Nb_2O_5 but

Table 1
Physicochemical properties of rutile TiO_2 and Nb_2O_5/TiO_2 heterojunctions.

Samples	Niobium loading[a]	TiO_2 size[b]	Nb_2O_5 size[c]	BET surface area
Rutile TiO_2	0%	32.1 nm	–	58.2 m^2 g^{-1}
Nb/Ti = 0.08	4.8%	33.2 nm	2.1 nm	56.7 m^2 g^{-1}
Nb/Ti = 0.12	7.2%	32.3 nm	2.2 nm	57.3 m^2 g^{-1}
Nb/Ti = 0.2	12.1%	30.5 nm	2.4 nm	56.8 m^2 g^{-1}
Nb/Ti = 0.4	23.9%	31.3 nm	2.5 nm	54.9 m^2 g^{-1}

[a] Determined by ICP.
[b] Estimated by Scherer equation from the broadening of rutile (110) reflection in XRD.
[c] Estimated by TEM observations.

ca. 0.9 eV higher than NbO_2 [25,26]. Based on the Nb 3d XPS results, we propose that niobium species exist in the form of electron-rich Nb_2O_5 in Nb_2O_5/TiO_2 heterojunctions. The excess electrons should come from the defect sites in TiO_2 support and Nb_2O_5-TiO_2 interaction (vide infra). Other important information we can obtain from XPS analysis is the surface composition of Nb_2O_5/TiO_2 heterojunctions in the depth up to several nanometers and surface niobium loadings are displayed in Fig. 2 (right). It is seen that surface niobium loading is obvious higher than bulk niobium loading determined by ICP (Table 1) and the surface niobium loading increases distinctly with increasing bulk Nb/Ti ratio, indicating the surface enrichment of homogeneously dispersed niobium species in Nb_2O_5/TiO_2 heterojunctions. Integrating the characterization results from XRD, Raman and TEM (vide infra), we can conclude that the in situ loaded niobium species on the surface rutile TiO_2 are well-dispersed amorphous Nb_2O_5 nanoparticles.

Diffuse reflectance UV–vis spectroscopy was performed to study the optical properties of rutile TiO_2, amorphous Nb_2O_5 and Nb_2O_5/TiO_2 heterojunctions. For rutile TiO_2, intrinsic absorption in the ultraviolet region attributed to the band-band transition is observed (Fig. 3) and the band gap energy is estimated to be 3.05 eV [10]. For amorphous Nb_2O_5, intrinsic absorption in the ultraviolet region attributed to the band-band transition is observed and gap energy is estimated to be 3.35 eV. While for Nb_2O_5/TiO_2 heterojunctions, intrinsic absorption in the ultraviolet region are also observed and the absorption edges appear in the region of 410–415 nm. That is to say, loading of Nb_2O_5 on the surface of TiO_2 does not significantly change the intrinsic absorption of rutile TiO_2 (the small red shift could be neglected). Besides, noticeable decreases in the light

absorption in ultraviolet region can be observed, which might be associated with interface charge transfer between TiO_2 and Nb_2O_5. In the Marcus theory, when the particle size of the semiconductor is very small (*e.g.* 3 nm), the electrons transfer across the semiconductor interface will be greatly accelerated and the apparent light absorption decreases [27].

Transmission electron microscopy (TEM) was employed to study the morphology of rutile TiO_2 and Nb_2O_5/TiO_2 heterojunctions, and the results are showed in Fig. 4. The average particle size of rutile TiO_2 particles is observed to be *ca.* 30 nm, in great consistence with XRD analysis results. For Nb_2O_5/TiO_2 heterojunctions, dark dots of 2–3 nm are clearly observed on the surface of rutile TiO_2 particles. Energy dispersive spectroscopy (EDS) analysis results confirm that the dark dots are niobium-containing species, *i.e.* Nb_2O_5 nanoparticles (Fig. 4f, Fig. S4). The Nb_2O_5 nanoparticles are uniform with very narrow size distributions, not so relevant with the niobium loading. Obviously, no core-shell structure can be detected even at high niobium loadings, in great contrast to literature reports [28].

For a direct view, some relevant physicochemical properties of rutile TiO_2 and Nb_2O_5/TiO_2 heterojunctions are summarized in Table 1.

Based on above-mentioned experimental results, the formation mechanism of Nb_2O_5/TiO_2 heterojunctions can be described as follows. In the first step, rutile TiO_2 nanoparticles are well dispersed in the strong acid solution (0.5 M HCl) with pH value of *ca.* 0.4, far away from the isoelectric point (IEP) of rutile TiO_2 particles (6–7) [29], which can provide a pledge for the homogeneous dispersion of Nb_2O_5 particles. Moreover, the surface of TiO_2 could be positively charged due to surface adsorption of proton [30], which can promote the absorptivity of anions on the surface of TiO_2. In the second step, when $NbCl_5$ is added into 30 mL 0.5 M hydrochloric acid solution, a series of negatively charged hydrolyzed products, such as $Nb(OH)_2Cl_4{}^-$ anions, come into being and clear solution is formed (Fig. 4h). In control experiments, $NbCl_5$ is added into 30 mL aqueous solution and a cloudy solution is obtained (Fig. 4g), indicating that water-insoluble niobium hydroxide is formed. Here the use of strong acidic mediate is a must to obtain clear solution containing niobium anions. In the mixed strong acidic solution containing both rutile TiO_2 and hydrolyzed niobium ions, negatively charged hydrolyzed niobium anions will absorb on the surface of TiO_2. In the last step, the mixture was heated to 100 °C to remove water
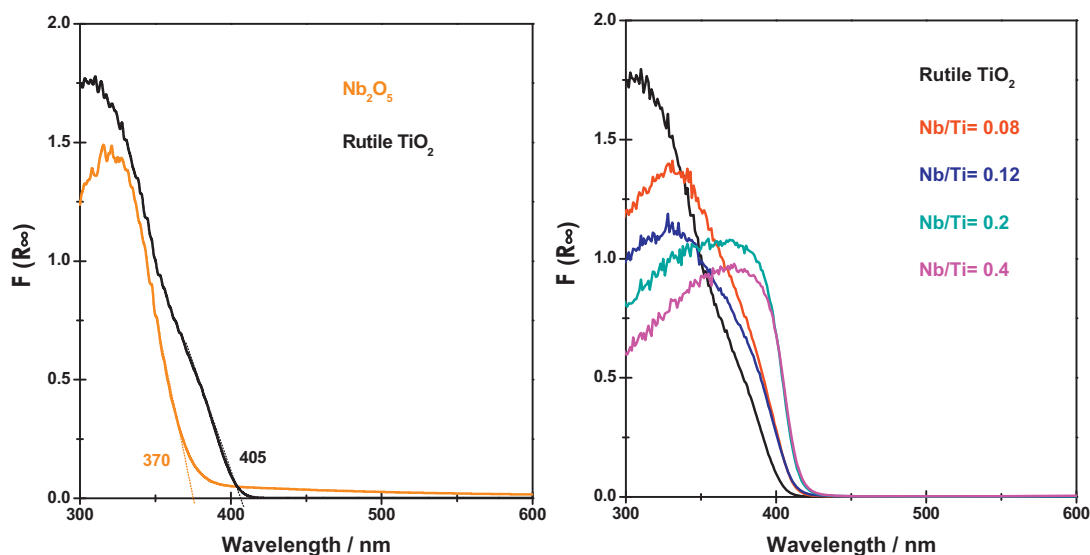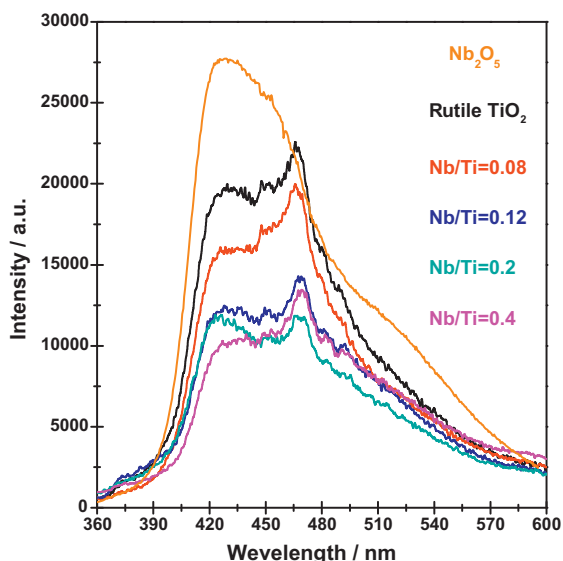

Fig. 3. UV–vis spectra of TiO_2, Nb_2O_5 and as-synthesized Nb_2O_5/TiO_2 heterojunctions.
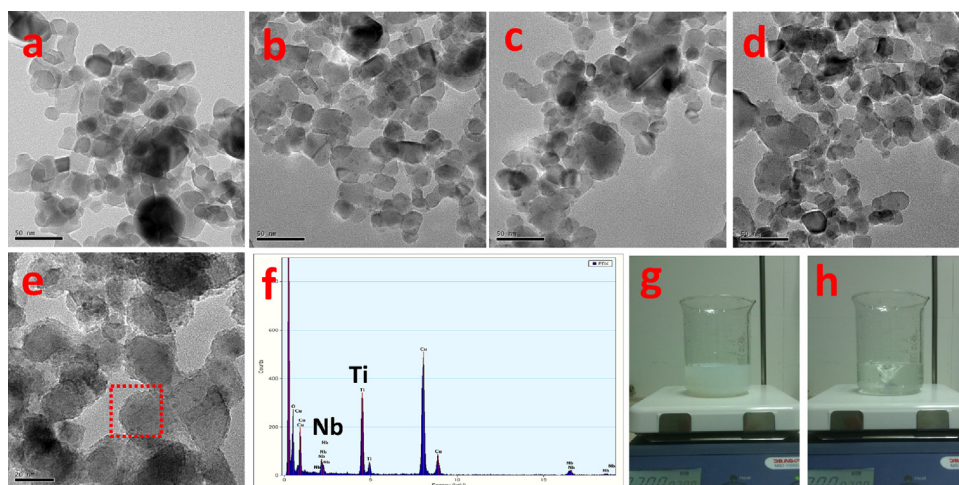
Fig. 4. TEM images of rutile TiO_2 (a) and Nb_2O_5/TiO_2 heterojunctions: Nb/Ti = 0.08 (b), Nb/Ti = 0.12 (c), Nb/Ti = 0.2 (d), Nb/Ti = 0.4 (e); EDS analysis on the red zone in e (f); Photographs of 0.5 g $NbCl_5$ in 30 mL distill water (g) and 0.5 M HCl aqueous solution (h).

Fig. 5. PL spectra of rutile TiO_2 and Nb_2O_5/TiO_2 heterojunctions recorded at room temperature.

and hydrochloric acid, and Nb_2O_5 nanoparticles are *in situ* loaded on the surface of rutile TiO_2.

PL spectroscopy is very useful to disclose the efficiency of charge carrier trapping, immigration and transfer in semiconductor. Generally, the PL emissions are originated from the radiative recombination of photo-generated electrons–holes [31–33]. Room temperature emission PL spectra of rutile TiO_2 and Nb_2O_5/TiO_2 heterojunctions are shown in Fig. 5. Two obvious signals at *ca.* 430 and 465 nm are observed for TiO_2 and all Nb_2O_5/TiO_2 heterojunctions, originated from the irradiative recombination of free electrons in shallow traps and sub-bands below conductive band and free holes at the valance band edge [32–34]. The intensities of the two PL signals are greatly reduced with the in situ loading of Nb_2O_5 on TiO_2 surface, indicating that heterojunctions formation can effectively suppress the irradiative recombination. Therefore, the Nb_2O_5/TiO_2 heterojunctions are expected to exhibit promoted activity in photocatalytic reactions.

Electron spin resonance (ESR) spectroscopy is employed to obtain more information about our Nb_2O_5/TiO_2 heterojunctions and the results are showed in Fig. 6. From the ESR results in the dark, only one weak peak ($g = 2.001$) is detected for pure rutile

TiO_2 and Nb_2O_5/TiO_2 (no signal can be detected for reference Nb_2O_5 sample), which should be attributed to O^- from O_2 dissociative adsorption onto the surface oxygen vacancy sites of TiO_2 [35,36]. After normalization, the intensity of the O^- signal decreases with increasing niobium loading on the surface of TiO_2, indicating the mask of the surface defect sites of TiO_2 by niobium loading [36]. That is, the surface defect sites of rutile TiO_2 are the nucleation centers for niobium precursor and the heterogeneous distribution of Nb_2O_5 are therefore ensured. This is the reason for the formation of electron-rich Nb_2O_5 as revealed by XPS analysis (Fig. 2).

On the other hand, more ESR signals appear for all samples under UV-Vis irradiation. The intense signals consisting of three sets of rhombic g values could be assigned to superoxide species (O_2^-: $g_1 = 2.002$, $g_2 = 2.009$, $g_3 = 2.028$), which are formed via the reduction of adsorbed O_2 by excited electrons [28]. After normalization, the intensities of the superoxide species on Nb_2O_5/TiO_2 heterojunctions are much higher than those on rutile TiO_2 and Nb_2O_5. For Nb_2O_5/TiO_2 heterojunctions, the intensities of superoxide species increase with increasing niobium loading, reach a maximum at Nb/Ti = 0.2, and then begin to decrease. The higher intensity of superoxide species corresponds to higher separation efficiency of photo-generated electron–hole pairs, in consistence with PL results in Fig. 5. Besides the superoxide species, two signals can be observed at $g = 1.982$ and 1.978 under irradiation, corresponding to the bulk Ti^{3+} species [28]. The higher intensities of bulk Ti^{3+} species may also indicate the higher separation efficiency of photo-generated electron–hole pairs on Nb_2O_5/TiO_2 heterojunctions than that on rutile TiO_2.

3.2. Photocatalytic activity of Nb_2O_5/TiO_2 heterojunctions

The photocatalytic activities of the as-prepared pure rutile TiO_2 and Nb_2O_5/TiO_2 heterojunctions are evaluated in the photocatalytic oxidation α-phenethyl alcohol, and the results are showed in Fig. 7. The selective photocatalytic oxidation of α-phenethyl alcohol can be achieved on all catalysts with selectivity of >95% to acetophenane (dehydroxylated toluene as detectable by-product), in accordance with our precious results over anatase and rutile TiO_2 [5]. The photocatalytic activities in Fig. 7 clearly indicate that Nb_2O_5/TiO_2 heterojunctions exhibit higher activity than pure rutile TiO_2 and Nb_2O_5. For Nb_2O_5/TiO_2 heterojunctions, the photocatalytic activity first increases with increasing niobium loading, reaches a maximal at Nb/Ti = 0.12 and then begins to decrease.
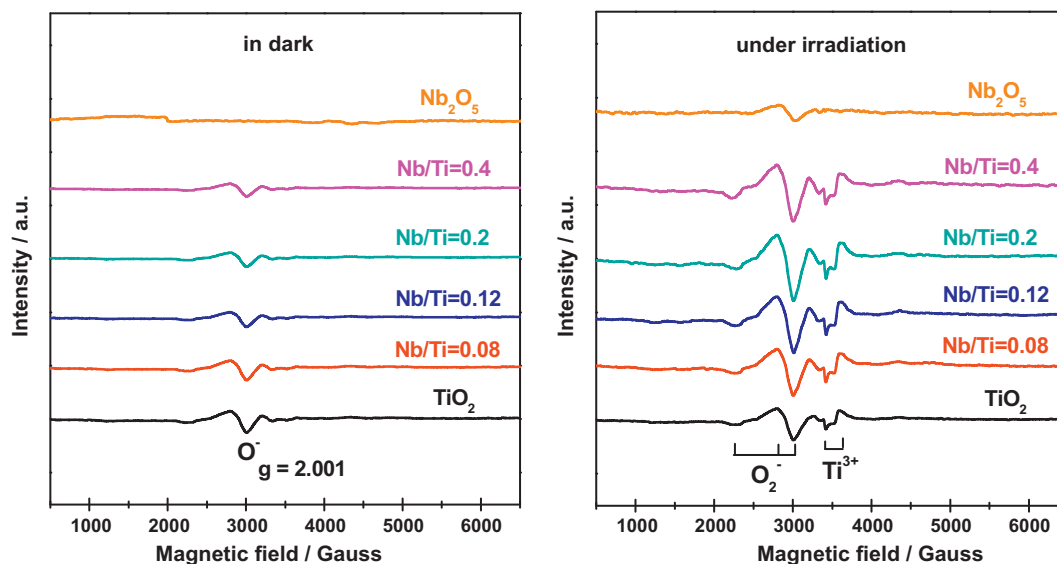
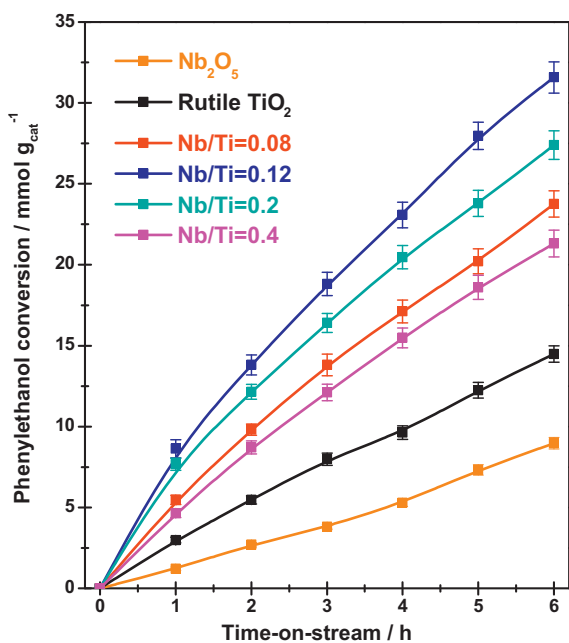**Fig. 6.** ESR spectra of TiO_2 and Nb_2O_5/TiO_2 heterojunctions in the dark and under irradiation.

Fig. 7. The photocatalytic oxidation α-phenylethanol over rutile TiO_2 and Nb_2O_5/TiO_2 heterojunctions under UV–Vis light irradiation; Reaction conditions: catalyst 0.3 g; α-phenethyl alcohol 25 mmol, benzotrifluoride 27 mL.

The highest α-phenethyl alcohol photocatalytic oxidation rate of *ca.* 8 mmol g_{cat}^{-1} h^{-1}, three times higher than rutile TiO_2 or eight times higher than Nb_2O_5, is obtained on Nb_2O_5/TiO_2 heterojunction at Nb/Ti = 0.12. Since the specific surface areas of all the samples are quite similar (Table 1), the mass specific activity can reflect the intrinsic activity, *i.e.* the surface specific activity [37], quite well.
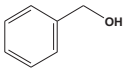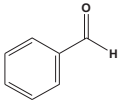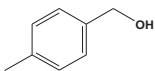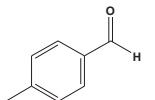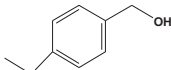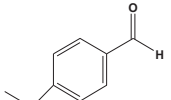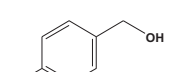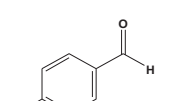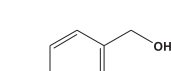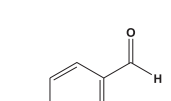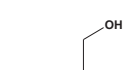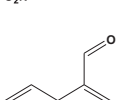
Our Nb_2O_5/TiO_2 heterojunctions also exhibit good recycling ability in the photocatalytic oxidation α-phenylethanol (results not shown here). XPS analysis results reveal that the existence states of niobium and titanium are kept unchanged after reaction (Fig. S5), confirming that Nb_2O_5/TiO_2 heterojunctions act as photocatalyst during reaction.

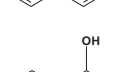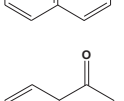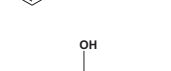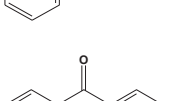Initiated by the superior activity of Nb_2O_5/TiO_2 heterojunctions for the photocatalytic oxidation of α-phenethyl alcohol, we further investigated the photocatalytic oxidation of various aromatic alcohols over Nb_2O_5/TiO_2. As shown in Table 2, Nb_2O_5/TiO_2 (Ni/Ti = 0.12) exhibits high activity for the photocatalytic oxidation of aromatic alcohols as well as good selectivity to carbonyl compounds in most cases. Exceptionally, the photocatalytic oxidation of diphenylmethanol over Nb_2O_5/TiO_2 is very slow because the adsorption of diphenylmethanol onto catalyst is difficult due to steric hindrance. For the photocatalytic oxidation of para-substituted benzyl alcohols, the activity is governed by the Hammett rule, *i.e.* substitution with electron-releasing groups –OCH_3 and –CH_3 increases the activity while substitution with electron-releasing groups –Cl and –NO_2 decreases the activity. In all cases, the photocatalytic activity of Nb_2O_5/TiO_2 is several times higher than reference rutile TiO_2, demonstrating the advantage of heterojunctions formation. It should be mentioned that aldehyde selectivity in the photocatalytic oxidation of primary aromatic alcohols is relatively low because the successive photocatalytic oxidation of product aldehydes to carboxylic acids and subsequent esterification between alcohols and carboxylic acids cannot be avoided under our reaction conditions.

The photocatalytic activities of the as-prepared pure rutile TiO_2 and Nb_2O_5/TiO_2 heterojunctions are also evaluated in the photocatalytic methanol reforming, and the results are showed in Fig. 8. Rutile TiO_2 (with 1 wt% Pt as co-catalyst) exhibits considerable photocatalytic activity in the methanol reforming, while amorphous Nb_2O_5 exhibits relatively lower photocatalytic activity, in consistence with literature reports [20,22,38,39]. For Nb_2O_5/TiO_2 heterojunctions, considerable hydrogen evolution rates from methanol reforming are observed and Nb/Ti ratios can influence the photocatalytic activity to some extent. Typically, the photocatalytic activity in methanol reforming first increases with increasing niobium loading, reaches a maximal at Nb/Ti ratio of 0.12 and then begins to decrease, similar to that in the photocatalytic oxidation α-phenylethanol. The highest hydrogen evolution rate of *ca.* 1.8 mmol g_{cat}^{-1} h^{-1} is obtained on Nb_2O_5/TiO_2 (Nb/Ti = 0.12), which is less than two times higher as rutile TiO_2 (1.0 mmol g_{cat}^{-1} h^{-1}). Comparing the activities of Nb_2O_5/TiO_2 heterojunctions in the photocatalytic oxidation α-phenylethanol and photocatalytic methanol reforming, we can conclude that heterojunctions can promote the photocatalytic activity in both reactions while the promotion effects are somewhat different, which will be discussed in the following section.

Table 2
Aerobic oxidation of aromatic alcohols over Nb_2O_5/TiO_2 and bare TiO_2[a].

Entry	Substrate	Product	Catalyst	Conversion (%)[b]	Selectivity (%)[c]	Reaction rate (mmol g_{cat}^{-1} h^{-1})
1	benzyl alcohol (–OH)	benzaldehyde (O, H)	Nb_2O_5/TiO_2	64.3	85.1	16.4
			TiO_2	21.6	91.4	5.4
2	4-methylbenzyl alcohol (–OH)	4-methylbenzaldehyde (O, H)	Nb_2O_5/TiO_2	66.2	84.9	17.1
			TiO_2	23.1	90.3	5.9
3	4-methoxybenzyl alcohol (O–, –OH)	4-methoxybenzaldehyde (O, H)	Nb_2O_5/TiO_2	67.8	74.3	17.6
			TiO_2	24.9	93.1	6.2
4	4-chlorobenzyl alcohol (Cl, –OH)	4-chlorobenzaldehyde (Cl, O, H)	Nb_2O_5/TiO_2	29.3	85.6	7.6
			TiO_2	10.2	91.5	2.7
5	4-nitrobenzyl alcohol (O_2N, –OH)	4-nitrobenzaldehyde (O_2N, O, H)	Nb_2O_5/TiO_2	12.3	83.9	3.6
			TiO_2	5.8	94.3	1.5
6	1-naphthalenemethanol (–OH)	1-naphthaldehyde (O)	Nb_2O_5/TiO_2	60.5	94.8	15.7
			TiO_2	24.2	96.7	7.2
7	α-phenylethanol (OH)	acetophenone (O)	Nb_2O_5/TiO_2	31.2	96.3	8.0
			TiO_2	13.1	97.2	2.6
8	benzhydrol (OH)	benzophenone (O)	Nb_2O_5/TiO_2	3.2	97.4	0.9
			TiO_2	0.9	98.1	0.3

[d] Calculated at aromatic alcohol conversion of 10–15%.
[a] Reaction conditions: 0.3 g catalyst, 25 mmol aromatic alcohol, 27 mL benzotrifluoride.
[b] Aromatic alcohol conversion at time-on-stream of 5 h.
[c] Aldehyde or ketone selectivity at time-on-stream of 5 h.

3.3. Factors controlling the photocatalytic activity of Nb_2O_5/TiO_2 heterojunctions

The UV–Vis spectra indicate the acceleration of electrons transfer across the semiconductor interface originated from the heterojunctions, which should be responsible for the promotion of photocatalytic activity of Nb_2O_5/TiO_2 heterojunctions compared with rutile TiO_2 or Nb_2O_5. However, over-high Nb/Ti ratio will lead to the decrease in the photocatalytic activity because too many heterojunctions can also act as the recombination sites for photo-generated electron–hole pairs [40]. As a balance of these two factors, a proper amount of heterojunctions should correspond to the best photocatalytic activity. In the present study, the Nb/Ti ratio of 0.12 could be optimized for Nb_2O_5/TiO_2 heterojunctions in both photocatalytic oxidation of α-phenylethanol (Fig. 7) and photocatalytic reforming of methanol (Fig. 8).

For amorphous Nb_2O_5 semiconductor, the conduction band potential is reported to be at least 0.2 eV positive, relative to anatase

TiO_2 [21,41]. However, the relative band edge positions between amorphous Nb_2O_5 and rutile TiO_2 have not been reported. So, we predict theoretically the band edge positions of the conduction band (E_{CB}) and valence band (E_{VB}) of the two semiconductors at the point of zero charge using the following empirical equation [42,43]:

$$E_{CB} = X - E^e - 0.5E_g$$

$$E_{VB} = E_g - E_{CB}$$

Here, X is the absolute electronegativity of the semiconductor, obtained from the geometric mean of the electronegativity of its constituent atoms (X values for Nb_2O_5 and TiO_2 are 5.55 and 5.81, respectively [43]); E_g is the band gap of the semiconductor; E^e is the energy of free electrons on the hydrogen scale (4.5 eV). The calculated conduction band edge potential of amorphous Nb_2O_5 (−0.45 eV) is more negative than that of rutile TiO_2 (−0.19 eV) and
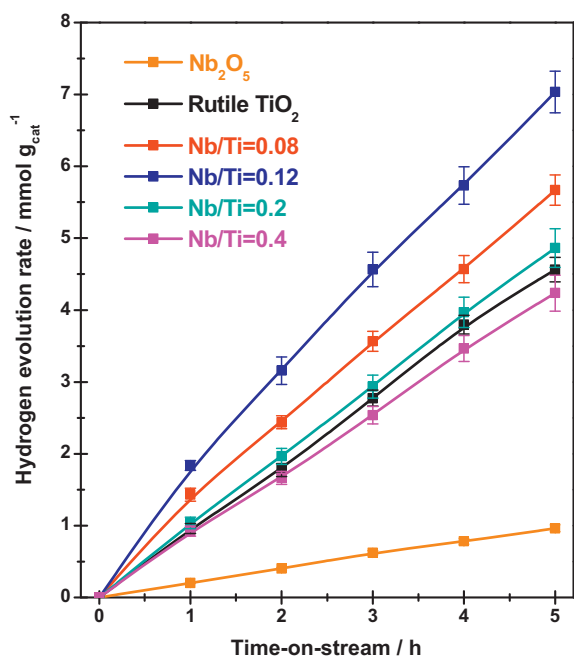
Fig. 8. Photocatalytic hydrogen evolution from methanol reforming over rutile TiO_2 and Nb_2O_5/TiO_2 heterojunctions under UV–vis light irradiation; 1 wt% Pt is *in situ* photo-deposited on the surface of samples.
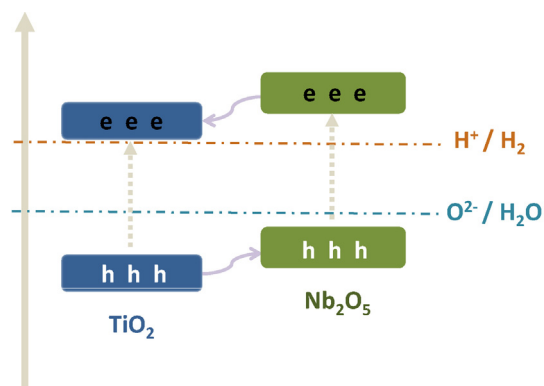
Fig. 9. Schematic diagram of Nb_2O_5/TiO_2 heterojunction and the relative conduction and valance band structure; Transfer directions of the photo-generated electrons and holes are also given.

the corresponding valence band edge potential of TiO_2 (2.81 eV) is more than that of Nb_2O_5 (2.75 eV). Therefore, when electron–hole pairs are created on semiconductor heterojunction upon ultravoilet light irradiation, the photo-generated electrons in the conduction band of Nb_2O_5 can transfer to rutile TiO_2, and the photo-generated holes are reversely transferred under the driving force of Fermi energy difference between the two semiconductors [14,44]. The schematic diagram of Nb_2O_5/TiO_2 heterojunction system and the transfer direction of the photo-generated electrons and holes are described in Fig. 9.

To further address the relative band structure of TiO_2 and Nb_2O_5 in this study, we measured the flat-band potentials using the electrochemical method [45,46] and the Mott–Schottky plots are shown in Fig. 10. It can be seen that both TiO_2 and Nb_2O_5 show positive slopes, confirming the fact that they are n-type semiconductors. Obviously, the E_{cb} of Nb_2O_5 is more negative than that of TiO_2, which is in good agreement with the data of the above-mentioned calculation results [47]. The Mott–Schottky plots of Nb_2O_5/TiO_2 heterojunctions are quite similar and the slope
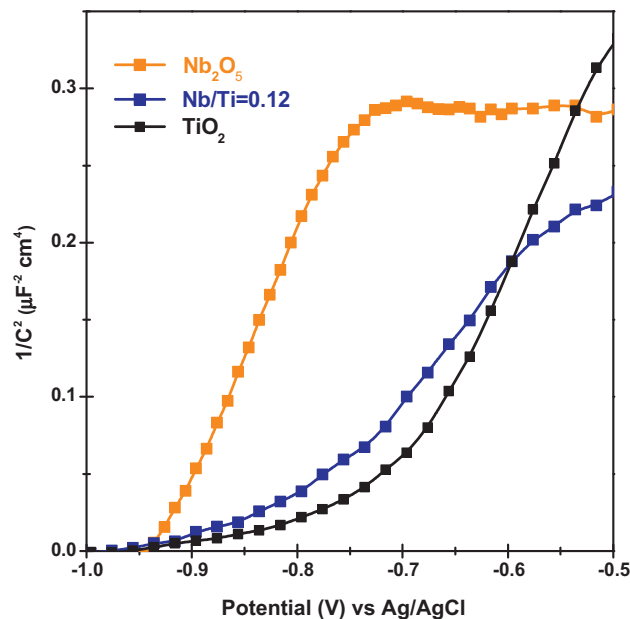
Fig. 10. Mott-Schottky plots of TiO_2, Nb_2O_5 and Nb_2O_5/TiO_2 heterojunction (Nb/Ti = 0.12) in 0.5 M Na_2SO_4.

(see example of Nb/Ti = 0.12) is smaller than TiO_2 or Nb_2O_5. According to previous reports [48], the smaller slope suggests a faster charge transfer. That is, the Mott–Schottky plots reveal that the charge transfer ability of Nb_2O_5/TiO_2 hereojunctions is higher than TiO_2 and Nb_2O_5, which will contribute to the higher photocatalytic activity.

When the heterojunctions are used in photocatalytic reduction reaction, *e.g.* photo-catalytic methanol reforming (reduction of H^+ to H_2), the photo-generated electrons will transfer from the conduction band of Nb_2O_5 to rutile TiO_2 and reduce $PtCl_6^{2-}$ to Pt sites on the surface of TiO_2, which subsequently act as the photocatalytic reduction sites. When the heterojunctions are used in photo-oxidation reaction, *e.g.* photocatalytic α-phenylethanol oxidation, the photo-generated holes will transfer from the valence band of TiO_2 to Nb_2O_5 and the small Nb_2O_5 nanoparticles will act as the photo-catalytic oxidation sites. Obviously, different sites are involved in the photocatalytic oxidation and reduction reactive reaction.

As a whole, it can be concluded that the as-prepared Nb_2O_5/TiO_2 heterojunctions system is suitable not only for photo-catalytic alcohol oxidation but also for proton reduction owing to the relative position of the conduction and valance band of the two components. While more significant promotion effect can be observed for photocatalytic alcohol oxidation due to the direct involvement of Nb_2O_5 nanoparticles in the reaction.

4. Conclusion

Ultra-fine Nb_2O_5 nanoparticles are successfully *in situ* loaded on rutile TiO_2 surface through a simple direct hydrolysis route under strong acidic conditions. Characterization results indicate that electron-rich amorphous niobium oxides of *ca.* 2 nm are well dispersed on the surface of TiO_2 and Nb_2O_5/TiO_2 heterojunctions are formed, which can greatly promote the separation efficiency of photo-generated electron–hole pairs under irradiation.

Nb_2O_5/TiO_2 heterojunctions exhibit remarkable photocatalytic activity, apparently higher than pure rutile TiO_2 or Nb_2O_5, in both the selective oxidation of α-phenylethanol and the hydrogen evolution from methanol reforming. The photocatalytic activity of Nb_2O_5/TiO_2 heterojunctions is dependent on Nb/Ti ratio and

the optimized activity can be obtained at Nb/Ti = 0.12, basically in accordance with the separation efficiency of photo-generated electron–hole pairs. The relative band edge positions between amorphous Nb_2O_5 and rutile TiO_2 are theoretically predicted and further confirmed by Mott–Schottky plots. According to the results, the photo-generated electrons in the conduction band of Nb_2O_5 will transfer to rutile TiO_2, and the photo-generated holes are reversely transferred under the driving force of Fermi energy difference between the two semiconductors. In this context, Nb_2O_5 nanoparticles in Nb_2O_5/TiO_2 heterojunctions act as oxidation sites and uncovered TiO_2 surfaces act as reduction sites in photocatalytic reactions.

Acknowledgements

Appendix A. Supplementary data

Supplementary material related to this article can be found, in the online version, at http://dx.doi.org/10.1016/j.apcatb.2014.01.049.

References

[1] A. Fujishima, K. Honda, Nature 238 (1972) 37–38.
[2] X.B. Chen, S.S. Mao, Chem. Rev. 107 (2007) 2891–2959.
[3] L. Thompson, J.T. Yates, Chem. Rev. 106 (2006) 4428–4453.
[4] M. Anpo, M. Takeuchi, J. Catal. 216 (2003) 505–516.
[5] J. Yan, G. Wu, N. Guan, L. Li, Z. Li, X. Cao, Phys. Chem. Chem. Phys. 15 (2013) 10978–10988.
[6] F. Zhang, R. Jin, J. Chen, C. Shao, W. Gao, L. Li, N. Guan, J. Catal. 232 (2005) 424–431.
[7] J. Yang, D. Wang, H. Han, C. Li, Acc. Chem. Res. 46 (2013) 1900–1909.
[8] E.S. Kim, N. Nishimura, G. Magesh, J.Y. Kim, J.W. Jang, H. Jun, J. Kubota, K. Domen, J.S. Lee, J. Am. Chem. Soc. 135 (2013) 5375–5383.
[9] M. Long, W. Cai, J. Cai, B. Zhou, X. Chai, Y. Wu, J. Phys. Chem. B 10 (2006) 20211–20216.
[10] A. Kudo, Y. Miseki, Chem. Soc. Rev. 38 (2009) 253–278.
[11] S.J. Hong, S. Lee, J.S. Jang, J.S. Lee, Energy Environ. Sci. 4 (2011) 1781–1787.
[12] X.F. Gao, W.T. Sun, Z.D. Hu, G. Ai, Y.L. Zhang, S. Feng, F. Li, L.M. Peng, J. Phys. Chem. C 113 (2009) 20481–20485.
[13] C.J. Li, P. Zhang, R. Lv, J.W. Lu, T. Wang, S.P. Wang, F.H. Wang, J.L. Gong, Small 9 (2013) 3951–3956.
[14] J.S. Zhang, M.W. Zhang, R.Q. Sun, X.C. Wang, Angew. Chem. Int. Ed. 51 (2012) 10145–10149.
[15] W.F. Yao, B. Zhang, C.P. Huang, C. Ma, X.L. Son, Q.J. Xu, J. Mater. Chem. 22 (2012) 4050–4055.
[16] L.C. Liu, X.R. Gu, C.Z. Sun, H. Li, Y. Deng, F. Gao, L. Dong, Nanoscale 4 (2012) 6351–6359.
[17] P. Chen, L. Gu, X.B. Cao, CrystEngComm 12 (2010) 3950–3958.
[18] H.L. Lin, H.F. Ye, B.Y. Xu, J. Cao, S.F. Chen, Catal. Comm. 37 (2013) 55–59.
[19] Y. Zhao, C. Eley, J.P. Hu, J.S. Foord, L. Ye, H.Y. He, S.C. Edman Tsang, Angew. Chem. Int. Ed. 51 (2012) 3846–3849.
[20] T. Ohuchi, T. Miyatake, Y. Hitomi, T. Tanaka, Catal. Today 120 (2007) 233–239.
[21] A.G.S. Prado, L.B. Bolzon, C.P. Pedroso, A.O. Moura, L.L. Costa, Appl. Catal. B 82 (2008) 219–224.
[22] H.Y. Lin, H.C. Yang, W.L. Wang, Catal. Today 174 (2011) 106–113.
[23] S.T. Aruna, S. Tirosh, A. Zaban, J. Mater. Chem. 10 (2000) 2388–2391.
[24] H.L. Ma, J.Y. Yang, Y. Dai, Y.B. Zhang, B. Lu, G.H. Ma, Appl. Surf. Sci. 253 (2007) 7497–7500.
[25] C.D. Wagner, W.M. Riggs, L.E. Davis, J.F. Moulder, G.E. Muilenberg, Handbook of X-ray Photoelectron Spectroscopy: A Reference Book of Standard Data for Use in X-ray Photoelectron Spectroscopy, Eden-Prairie, Perkin-Elmer MN, 1979.
[26] V.L.S.T. da Silva, M. Schmal, S.T. Oyama, J. Solid State Chem. 123 (1996) 169–182.
[27] P.V. Kamat, J. Phys. Chem. Lett. 3 (2012) 663–672.
[28] S. Furukawa, T. Shishido, K. Teramura, T. Tanaka, ACS Catal. 2 (2012) 175–179.
[29] F.X. Zhang, N.J. Guan, Y.Z. Li, X. Zhang, J.X. Chen, H.S. Zeng, Langmuir 19 (2003) 8230–8234.
[30] B. Ohtani, Y. Okugawa, S. Nishimoto, T. Kagiya, J. Phys. Chem. 91 (1987) 3550–3555.
[31] A. Suisalu, J. Aarik, H. Mandar, I. Sildos, Thin Solid Films 336 (1998) 295–298.
[32] B. Liu, X. Zhao, Q. Zhao, X. He, J. Feng, J. Electron Spectrosc. Relat. Phenom. 148 (2005) 158–163.
[33] R.E. Rex, F.J. Knorr, J.L. McHale, J. Phys. Chem. C 117 (2013) 7949–7951.
[34] W. Feng, G.J. Wu, L.D. Li, N.J. Guan, Green Chem. 13 (2011) 3265–3272.
[35] Y. Shiraishi, D. Tsukamoto, Y. Sugano, A. Shiro, S. Ichikawa, S. Tanaka, T. Hirai, ACS Catal. 2 (2012) 1984–1992.
[36] J. Yan, G. Wu, N. Guan, L. Li, Chem. Commun. 49 (2013) 11767–11769.
[37] J. Zhang, Q. Xu, Z.C. Feng, M.J. Li, C. Li, Angew. Chem. Int. Ed. 47 (2008) 1766–1769.
[38] K. Sayama, H. Arakawa, K. Domen, Catal. Today 28 (1996) 175–182.
[39] I. Nowak, M. Ziolek, Chem. Rev. 99 (1999) 3603–3624.
[40] D. Robert, Catal. Today 122 (2007) 20–26.
[41] H.L. Luo, W.J. Song, P.G. Hoertz, K. Hanson, R. Ghosh, S. Rangan, M.K. Brennaman, J.J. Concepcion, R.A. Binstead, R. Bartynski, R. Lopez, T.J. Meyer, Chem. Mater. 25 (2013) 122–134.
[42] M.A. Butler, D.S. Ginley, J. Electrochem. Soc. 125 (1978) 228–232.
[43] Y.I. Kim, S.J. Atherton, E.S. Brigham, T.E. Mallouk, J. Phys. Chem. 97 (1993) 11802–11810.
[44] J. Tersoff, Phys. Rev. B 30 (1984) 4874–4877.
[45] H. Huang, D. Li, Q. Lin, Y. Shao, W. Chen, Y. Hu, Y. Chen, X. Fu, J. Phys. Chem. C 113 (2009) 14264–14269.
[46] Y. Jia, S. Shen, D. Wang, X. Wang, J. Shi, F. Zhang, H. Han, C. Li, J. Mater. Chem. A 1 (2013) 7905–7912.
[47] S.R. Morrison, Electrochemistry at Semiconductor and Oxidized Metal Electrodes, Plenum Press, New York, 1980 (Chapter 4).
[48] F. Su, T. Wang, R. Lv, J. Zhang, P. Zhang, J. Lu, J. Gong, Nanoscale 5 (2013) 9001–9009.